An Approximated, Control Affine Model for a Strawberry Field Scouting Robot Considering Wheel–Terrain Interaction

Pablo Menendez-Aponte†, Xiangling Kong†*,
and Yunjun Xu‡

† *Graduate Research Assistant, Mechanical and Aerospace Engineering, University of Central Florida, Orlando, FL, 32816, USA. E-mail: olbap323@gmail.com*
‡ *Professor, Mechanical and Aerospace Engineering, University of Central Florida, Orlando, FL, 32816, USA. E-mail: yunjun.xu@ucf.edu*

SUMMARY
Recently, autonomous field robots have been investigated as a labor-reducing means to scout through commercial strawberry fields for disease detection or fruit harvesting. To achieve accurate over-bed and cross-bed motions, it is preferred to design the motion controller based on a precise dynamic model. Here, a dynamic model is developed for a custom-designed strawberry field robot considering terramechanic wheel–terrain interaction. Different from existing models, a torus geometry is considered for the wheels. In order to obtain a control affine model, the longitudinal force is curve-fitted using a polynomial function of the slip/skid ratio, while the lateral force is curve-fitted using an exponential function of both the slip/skid ratio and slip angle. An extended Kalman filter (EKF) is then developed to estimate the unknown parameters in the approximated model such that the state variables propagated by such a model can match experimental data. The approximated model and the EKF-based parameter estimation method are then validated in a commercial strawberry farm.

KEYWORDS: Wheel–terrain interaction model (WTIM); Wheeled mobile robot (WMR); Field robot; Extended Kalman filter (EKF).

1. Introduction
Emerging robotic techniques in agriculture have recently become the focus of much attention. Robotics can be used in agriculture to reduce labor costs and enhance farming efficiency, thus increasing profitability. WinterGreen Research, a private research company, published a study entitled "Agricultural Robots Market Shares, Worldwide, 2014 to 2020," which predicted that the agricultural robot market will expand from $817 million in 2013 to $16.3 billion by 2020.[1] Furthermore, WinterGreen Research predicted that while many unmanned aerial vehicles have been previously put to use in agricultural research, autonomous wheeled mobile robots (WMRs) will ultimately be more useful in this field.[1] This expansion in the number of mobile robots used in agriculture is believed to be a consequence of the increased size of modern commercial farms. It is no longer feasible for human workers to cover an entire field by foot in a single 8-h work day. Furthermore, the structured nature of many commercial agricultural fields makes them ideal for robotic scouts that can efficiently work long hours over large distances. Autonomous robotics could enhance farm productivity in every stage of crop cultivation from planting to harvesting.

* Corresponding author. E-mail: xl.kong@knights.ucf.edu

In recent years, many advances in robotics have closed the technological gaps required to make agricultural mobile robots work efficiently in farms. For instance, low-cost ultrasonic range finders were utilized in the design of a row guidance system for a white asparagus harvesting robot.[2] Penetrometer devices were used with ground robot to analyze the soil compaction and create 3D soil maps.[3] Machine vision has been used in strawberry harvesting[4] and corn's nitrogen deficiency detection.[5] Spectroscopic imaging, a subfield of machine vision, has been widely used in rapid disease detection.[6] Despite these advances, there are still problems that must be solved before fully automated agriculture operations can be realized. One critical need in off-road robots is the dynamic modeling of such robots in loose terrain. While there are several techniques available for modeling a wheeled vehicle's dynamic motion in loose terrain, they are computationally expensive and the obtained models are not suitable for controller designs.

In the past, control and localization schemes for WMRs traveling on hard surfaces have been accomplished for no-slip, non-holonomic wheel cases.[7,8] Researchers have been able to successfully apply the no slip constraint to autonomous robots in agriculture,[2] but these robots were not required to do any radical maneuvers. In contrast, slipping and skidding will naturally occur when a robot makes sharp turns. A navigation estimation scheme must then be designed, as traditional control schemes based on the no-slip constraint are inappropriate for these maneuvers. In loose terrains, wheel slip ratio and slip angle play critical roles in the dynamics of WMRs of all configurations. In refs. [9, 10], the authors use a kinematic constraint for a four-wheel skid steer robot that is borrowed from the design of treaded ground vehicles. This constraint uses data collected experimentally to relate the slip/skid ratio to the yaw rate of the vehicle. While the authors have shown success in experiments, such a constraint is purely empirical and has no physical foundation, making it unpredictable for new terrain types. Furthermore, this kinematic constraint completely neglects the slip angle.

The research conducted in this paper was carried out with a strawberry orchard scout robot in mind. The realization of a robotic scout for disease detection in strawberry orchards has several control system design criteria that have not been addressed by previous works. Commercial strawberry orchards are grown in organized plasticulture rows that can range in size and spacing. From the authors' experience in three commercial fields in Florida, the beds generally range in size from 52.42 to 100 cm and are spaced from 45.72 to 55.88 cm apart. These dimensions will require a tight turning radius of approximately 81.28 cm during cross-bed motion maneuvers. Additionally, the three leading states for strawberry production, California, Florida, and Oregon,[11] have different climates and topologies. With this in mind, the paper presents an approximated wheel–terrain interaction model (WTIM) suitable for controller designs under tight turns when slipping/skidding are at their highest, and furthermore presents an estimation scheme for unknown parameters in the derived approximated model. Here, "parameter estimation" refers to identifying a set of parameter values such that the state variables propagated via the approximated model can match well with the experimental data, adapting to new field environments.

We begin with the terramechanic WTIM, first developed in the 1950s by Bekker and later on by Wong.[12,13] The terramechanic WTIM has become popular for off-road vehicle designs due to its accuracy and reduced computational cost when compared with finite element methods. In terms of controllability, however, terramechanic WTIMs are not analytical and thus cannot easily be implemented in control or guidance designs. Here terramechanic WTIMs are utilized to gain a more fundamental understanding of the dominant forces that can characterize a mobile robot's dynamics in off-road terrains. The main contributions of this study are as follows: (i) a torus-shaped wheel is considered when deriving the WTIM; (ii) the full WTIM is curve fitted to achieve an approximated, control affine model; and (iii) the unknown parameters in this approximated model are estimated via an extended Kalman filter (EKF).

This paper is organized as follows. In Section 2, the rigid body dynamics model for an agricultural field robot is shown. In Section 3, a terramechanic method for calculating the terrain reaction forces on a torus-shaped wheel is presented. In Section 4, an approximated WTIM is derived via a curve fitting method. In Section 5, an EKF is designed to estimate the unknown parameters in the approximated WTIM. In Section 6, the parameter estimation scheme and the approximated model are validated through a scouting motion experiment crossing three strawberry beds in a commercial strawberry farm. Conclusions are given in Section 7.
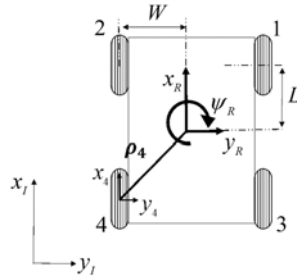
Fig. 1. View of robot displaying the inertial and body fixed coordinates.

2. Skid Steer Kinematics and Field Robot 2-D Dynamics

2.1. Reference frames
A diagram of the field robot is shown in Fig. 1. The robot is assumed to travel on a fixed horizontal plane, thus the complete posture of the robot can be defined in an inertial reference frame Ω_I by two position coordinates (x_I, y_I) and a heading angle ψ_R. Here the subscript I denotes the inertial reference frame and the subscript R denotes the body fixed frame Ω_B placed at the center of mass of the robot. Accompanying Ω_I and Ω_B are four local wheel reference frames, (x_i, y_i), $i = 1, 2, 3, 4$. The local wheel reference frames Ω_i are fixed in Ω_B and share the same orientation. The distance from the origin of Ω_B to the origin of Ω_i is denoted by the position vector ρ_i, $i = 1, 2, 3, 4$. W is the distance from the robot center of mass to the wheel center of mass along the body fixed y-axis. Likewise, L refers to the distance from the robot center of mass to the wheel center of mass along the body fixed x-axis.

2.2. Skid-Steer kinematics
The wheels are grouped into the right and left wheel banks. For example, the right wheel bank shown in Fig. 1 consists of wheels 1 and 3, whereas the left wheel bank consists of wheels 2 and 4. As opposed to separate descriptions for each wheel, some of the wheel kinematics can be described in terms of the wheel banks. For instance, the right and left wheel bank angular velocities are $\omega_r = \omega_1 = \omega_3$ and $\omega_l = \omega_2 = \omega_4$, respectively. The longitudinal velocities of the right and left wheel banks can be written in their respective local reference frames as

$$\dot{x}_r = \dot{x}_1 = \dot{x}_3 = \dot{x}_R - W\dot{\psi}_R$$
$$\dot{x}_l = \dot{x}_2 = \dot{x}_4 = \dot{x}_R + W\dot{\psi}_R \tag{1}$$

and the lateral velocities of the wheels are

$$\dot{y}_1 = \dot{y}_2 = \dot{y}_R + L\dot{\psi}_R$$
$$\dot{y}_3 = \dot{y}_4 = \dot{y}_R - L\dot{\psi}_R \tag{2}$$

2.3. Equations of motion
Let $(\ddot{x}_R, \ddot{y}_R, \ddot{\psi}_R)$ be the longitudinal, lateral, and yaw accelerations of the robot in the body fixed frame Ω_B. The equation of motion of the robot can be derived as

$$\ddot{x}_R = \dot{\psi}_R \dot{y}_R + \sum F_{w,x}/m$$
$$\ddot{y}_R = -\dot{\psi}_R \dot{x}_R + \sum F_{w,y}/m \tag{3}$$
$$\ddot{\psi}_R = \sum M_{ext}/I_z,$$

where m is the mass of the robot, I_z is the moment of inertia about the z-axis, $\sum F_{w,x}$, $\sum F_{w,y}$, and $\sum M_{ext}$ are the summations of forces and moments due to wheel–terrain interactions.
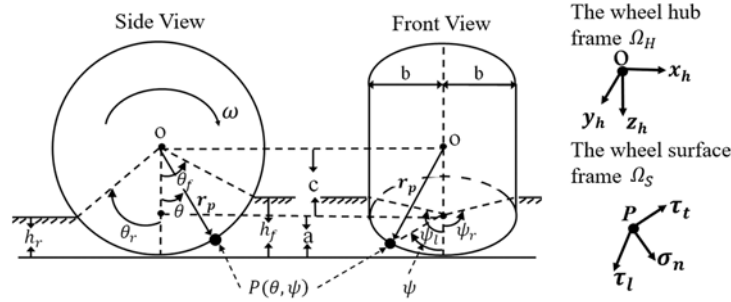
Fig. 2. Side view and front view of a wheel with respect to loose terrain.

Assumption 2.1. *For scouting in strawberry fields, high-speed maneuvering is not required; thus constant wheel loads are assumed and aerodynamic forces are neglected in the model.*

3. Individual WTIM

3.1. Terramechanics model for wheel–terrain interaction

Here the terrain reaction forces on an individual wheel are derived, mainly using the terramechanic method.[14] In the past, terramechanic models have been utilized in the design of terrestrial rovers, which use wheels with a cylindrical shape.[15] For a typical agricultural field robot, the wheel has a torus or donut shape. The bulldozing forces are not needed for the torus-shaped wheels in contrast with the cylindrical-shaped wheels.[14,15] However, two extra coordinate transformations need to be included in the integrals when the terrain reaction forces are computed for torus-shaped wheels. This section focuses on the WTIM for an individual wheel. Therefore for clarity and brevity, the subscript associated with wheels 1, 2, 3, and 4 is omitted.

3.1.1. Torus geometry and sinkage depth. The surface of a torus is generated by revolving an ellipse around an axis coplanar with the ellipse. As shown in Fig. 2, the wheel hub reference frame Ω_H is defined at the center of wheel hub O, where the x_h-axis is parallel to the horizontal plane and points towards the wheel movement and the z_h-axis points vertically downward. For an arbitrary point P on the interaction surface of the wheel, the wheel surface reference frame Ω_S includes τ_t, τ_l, and σ_n as the tangential, lateral, and normal directions, respectively.

In Fig. 2, ω is the individual wheel angular velocity. The entry and exit sinkage depths, h_f and h_r, are defined as the distances a wheel penetrates the terrain, which affect the contact patch or the region of the wheel surface that makes contact with the terrain. As will be seen in the derivation of the terramechanic WTIM, it is convenient to describe the contact patch by four angles: the entry angle θ_f, the exit angle θ_r, the right bound angle ψ_r, and the left bound angle ψ_l. The right bound and the left bound angles, ψ_r and ψ_l, are defined as the angles from the wheel rim depressed into the soil at the center of the wheel to the right and left surfaces of the soil at the wheel sidewalls, respectively. The computation of these angles is based on ref. [14], as listed in Appendix A. An arbitrary point P on the torus surface can be expressed by the position vector r_p from the wheel hub center[16] as

$$r_p = \begin{bmatrix} (c + a\cos\psi)\sin\theta \\ b\sin\psi \\ (c + a\cos\psi)\cos\theta \end{bmatrix}, \tag{4}$$

where c is the major radius, a is the minor radius, and b is half of the torus width. The angles of revolution θ and ψ are shown in Fig. 2.

3.1.2. Wheel–terrain interaction forces. The force acting on a steadily rotating wheel, $F_w = \begin{bmatrix} F_{w,x}, F_{w,y}, F_{w,z} \end{bmatrix}^T$, can be found by integrating the tangential, lateral, and normal stress components along the wheel–terrain contact patch[12,13,17] as
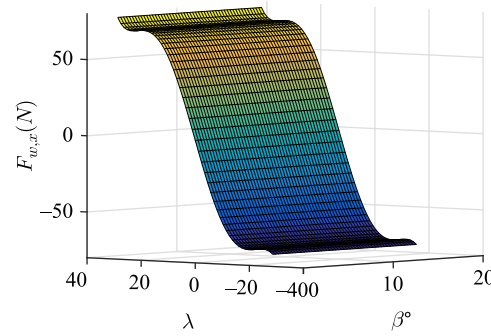
Fig. 3. Longitudinal reaction force simulated using the full WTIM with a torus shape.

$$F_{w,x} = \int_{\psi_l}^{\psi_r} \int_{\theta_r}^{\theta_f} \left[(\tau_t \cos\theta + \tau_l \sin\psi \cos\theta + \sigma_n \cos\psi \sin\theta) \, d \right] d\theta d\psi$$

$$F_{w,y} = \int_{\psi_l}^{\psi_r} \int_{\theta_r}^{\theta_f} \left[(\tau_l \cos\psi - \sigma_n \sin\psi) \, d \right] d\theta d\psi \quad (5)$$

$$F_{w,z} = \int_{\psi_l}^{\psi_r} \int_{\theta_r}^{\theta_f} \left[(-\tau_t \sin\theta + \tau_l \sin\psi \cos\theta + \sigma_n \cos\psi \cos\theta) \, d \right] d\theta d\psi,$$

where $d \triangleq (c + a \cos\psi) \sqrt{a^2 \sin^2\psi + b^2 \cos^2\psi}$. The computation of τ_t, τ_l, and σ_n is based on refs. [14, 17] and a brief derivation of these terms included is in Appendix A. It is worth mentioning that for the planar motion in this study, the z-direction reaction force $F_{w,z}$ is not shown in the dynamic model.

3.1.3. Slip/Skid ratio and slip angle. The effects of wheel slip/skid ratio λ and slip angle β on the longitudinal and lateral terrain reaction forces are investigated for a wheel under constant load (Assumption 2.1). The wheel slip/skid ratio refs. [14, 17] is expressed as

$$\lambda = \begin{cases} (r\omega - \dot{x}) / (r\omega), & |\dot{x}| \le |r\omega| \\ (r\omega - \dot{x}) / \dot{x}, & |\dot{x}| > |r\omega| \end{cases}, \quad (6)$$

where $\dot{x}$ is the wheel longitudinal velocity expressed in Ω_H, and r is the radius of the individual wheel. The numerator here is the difference between the ideal wheel velocity under a no-slipping or -skidding condition and the actual wheel velocity $\dot{x}$.

The wheel slip angle refs. [14, 17] β is the angle between the longitudinal and lateral velocity components of the wheel as

$$\beta = \tan^{-1}(\dot{y}/\dot{x}), \quad (7)$$

in which $\dot{y}$ is the lateral velocity components of an individual wheel.

3.1.4. Terramechanics WTIM simulation. The derived WTIM is simulated for single-wheel, linear motion. The simulation results are used to analyze the relationships among slip/skid ratio, slip angle, longitudinal force, and lateral force. The parameters related to off-road soils are taken from ref. [18] as listed in Table A1 of Appendix A. The longitudinal and lateral forces are evaluated as the slip ratio varies from -0.5 to 0.5 and the slip angle varies from $0°$ to $16°$ following refs. [14, 18].

As shown in Fig. 3, the longitudinal force $F_{w,x}$ varies significantly with respect to the slip ratio λ due to the changing shear deformation, while it maintains relatively stationary when the slip angle β changes. It can be seen in Fig. 4 that the lateral force $F_{w,y}$ depends not only on λ but also on β. It is worth noting that the simulation results achieved here match well with the results shown in ref. [14].

Table I. Goodness of fit for the longitudinal force in the approximated WTIM.

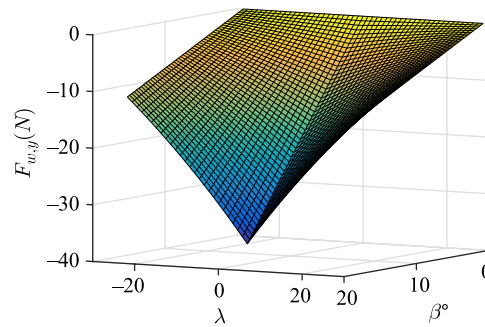| Polynomial	Slip angle	$\beta = 4°$	$\beta = 8°$	$\beta = 12°$	$\beta = 16°$
Third order	MAE	0.7366	0.6491	0.5311	0.4204
	R-square	0.9887	0.9923	0.9956	0.9977
Fourth order	MAE	0.5110	0.4433	0.3672	0.3174
	R-square	0.9955	0.9970	0.9982	0.9989
Fifth order	MAE	0.1575	0.1379	0.1452	0.1709
	R-square	0.9994	0.9995	0.9996	0.9996
Sixth order	MAE	0.1267	0.1394	0.1526	0.1748
	R-square	0.9996	0.9996	0.9996	0.9996

Fig. 4. Lateral reaction force simulated using the full WTIM with a torus shape.

3.2. Approximated WTIM

While the terramechanic model shown in Section 3.1 allows for accurate simulation and analysis of the wheel–terrain interaction forces in soft terrain, it does not have a control affine format[10, 13, 19] and thus is not convenient for guidance, navigation, and control design. Also, the full WTIM is computationally expensive. A large body of research has shown that λ and β are two critical elements in off-road wheel–terrain interactions.[9, 10, 14, 15, 17–21] Based on Fig. 3, a polynomial function is used to approximate the longitudinal force $F_{w,x}$ as

$$F_{w,x} = \sum_{i=0}^{k} c_i \lambda^k, \tag{8}$$

where c_i, $i = 0, 1, ..., k$ are the parameters of the polynomial function.

Observing the trend of lateral force in Fig. 4, $F_{w,y}$ decreases when the slip ratio λ increases and increases along β increases. Thus we approximate $F_{w,y}$ as

$$F_{w,y} = -d_1 \beta \left(d_2 + e^{-d_3 \lambda} \right), \tag{9}$$

where d_1, d_2, and d_3 are the parameters to be identified.

Two criteria are used to quantify the performance of the approximation: the mean absolute error (MAE)[24] and the R-square[25] value. In Table I, it can be seen that the fourth-order polynomial's MAE value is the lowest, while the R-square value increases as the order of the polynomial fit increases. However, it is worth mentioning that a higher order polynomial will have higher computational costs and will introduce more parameters which must be identified. Therefore, a fourth-order polynomial was chosen to approximate the longitudinal force in this study. Table II lists the performance of the approximation for the lateral force. Here, the MAE values are below 0.15, while the R-square values are all above 0.99 for each slip angle case. Thus, we can argue that the approximated WTIM longitudinal force and lateral force can be used when controlling the field robot. Any approximation errors can be handled by a well-tuned robust or adaptive controller. It is worth noting that the parameters obtained off-line via the least squares approach can be used as initial guesses; the actual values can vary with terrain conditions and should be identified online via the EKF, discussed in a later section.

Table II. Goodness of fit for the lateral force in the approximated WTIM.

Evaluation / Slip angle	$\beta = 4°$	$\beta = 8°$	$\beta = 12°$	$\beta = 16°$
MAE	0.0213	0.0351	0.0585	0.1254
R-square	0.9999	0.9999	0.9998	0.9996

4. Approximated Control Affine Model

Based on the approximated longitudinal force in Eq. (8) and the lateral force in Eq. (9), the four-wheel skip–skid robot can be modeled as the following nonlinear control affine model:

$$\dot{x} = f(x) + g(x)u, \tag{10}$$

where $x \in \Re^{11 \times 1}$, $u \in \Re^{2 \times 1}$, $f(x) \in \Re^{11 \times 1}$, and $g(x) \in \Re^{11 \times 2}$ are the state vector, control variables, state function, and control input matrix, respectively. Here x is chosen to be

$$x = \left[\dot{x}_R, \ \dot{y}_R, \ \dot{\psi}_R, \ \omega_r, \ \omega_l, \ \lambda_r, \ \lambda_l, \ \beta_1, \ \beta_2, \ \beta_3, \ \beta_4 \right]^T, \tag{11}$$

where $\dot{\psi}_R$ is the yaw rate of the robot. The commands to the right and left wheel banks, $\omega_{c,r}$ and $\omega_{c,l}$, are included in the control variables $u \in \Re^{2 \times 1}$ as

$$u = \left[\omega_{c,r}, \ \omega_{c,l} \right]^T \tag{12}$$

Using Eqs. (3), (8), and (9), the motion of the field robot is governed by

$$
\begin{aligned}
\ddot{x}_R &= \dot{\psi}_R \dot{y}_R + 2 \sum_{i=0}^{k} c_i \left(\lambda_r^k + \lambda_l^k \right) / m \\
\ddot{y}_R &= -\dot{\psi}_R \dot{x}_R - d_1 \left[k_r \left(\beta_1 + \beta_3 \right) + k_l \left(\beta_2 + \beta_4 \right) \right] / m \\
\ddot{\psi}_R &= \left\{ 2W \sum_{i=0}^{k} c_i \left(\lambda_l^k - \lambda_r^k \right) + d_1 L \left[k_r \left(\beta_3 - \beta_1 \right) + k_l \left(\beta_4 - \beta_2 \right) \right] \right\} / I,
\end{aligned}
\tag{13}
$$

where $k_r \triangleq d_2 + e^{-d_3 \lambda_r}$ and $k_l \triangleq d_2 + e^{-d_3 \lambda_l}$, respectively. The angular velocities of the wheel banks are regulated by a well-tuned Proportional-Integral-Derivative (PID) controller and governed by the following first-order ordinary differential equation

$$\dot{\omega}_j = k_\omega \left(\omega_{c,j} - \omega_j \right), \quad j = r, l, \tag{14}$$

where k_ω is a motor time constant that can be found experimentally. The state equations for the right and left wheel slip/skid ratios are found by taking the time derivative of Eq. (6) as

$$\dot{\lambda}_j = f_{\lambda,j} + g_{\lambda,j} \omega_{c,j}, \quad j = r, l, \tag{15}$$

in which

$$f_{\lambda,j} = \begin{cases} -\omega_j r \left(k_\omega \dot{x}_j + \ddot{x}_j \right) / (r^2 \omega_j^2), & |\omega_j r| \geq |\dot{x}_j| \\ -\omega_j r \left(k_\omega \dot{x}_j + \ddot{x}_j \right) / \dot{x}_j^2, & |\omega_j r| < |\dot{x}_j| \end{cases} \quad j = r, l. \tag{16}$$

and

$$g_{\lambda,j} = \begin{cases} r k_\omega \dot{x}_j / (r^2 \omega_j^2), & |\omega_j r| \geq |\dot{x}_j| \\ r k_\omega \dot{x}_j / \dot{x}_j^2, & |\omega_j r| < |\dot{x}_j| \end{cases}, \quad j = r, l. \tag{17}$$

Taking the time derivative of Eq. (7), the state equation for the slip angle can be derived as

$$\dot{\beta}_i = \left(\dot{x}_i \ddot{y}_i - \dot{y}_i \ddot{x}_i \right) / \left(\dot{y}_i^2 + \dot{x}_i^2 \right), \quad i = 1, 2, 3, 4, \tag{18}$$

where $\dot{x}_i$ and $\dot{y}_i$ can be found in Eqs. (1) and (2), respectively. The longitudinal and lateral accelerations $\ddot{x}_i$ and $\ddot{y}_i$ of the ith wheel in the inertial frame Ω_I can be obtained by

$$
\begin{aligned}
\ddot{x}_1 &= \ddot{x}_3 = \ddot{x}_R - W\ddot{\psi}_R \\
\ddot{x}_2 &= \ddot{x}_4 = \ddot{x}_R + W\ddot{\psi}_R \\
\ddot{y}_1 &= \ddot{y}_2 = \ddot{y}_R + L\ddot{\psi}_R \\
\ddot{y}_3 &= \ddot{y}_4 = \ddot{y}_R - L\ddot{\psi}_R
\end{aligned}
\tag{19}
$$

Combining all the aforementioned equations, the state function $f(x)$ is

$$
f(x) =
\begin{bmatrix}
\dot{\psi}_R \dot{y}_R + 2\left[\sum_{i=0}^{k} c_i\left(\lambda_r^k + \lambda_l^k\right)\right]/m \\
-\dot{\psi}_R \dot{x}_R - d_1\left[k_r\left(\beta_1 + \beta_3\right) + k_l\left(\beta_2 + \beta_4\right)\right]/m \\
\left\{2W\sum_{i=0}^{k} c_i\left(\lambda_l^k - \lambda_r^k\right) + d_1 L\left[k_r\left(\beta_3 - \beta_1\right) + k_l\left(\beta_4 - \beta_2\right)\right]\right\}/I \\
-k_\omega \omega_r \\
-k_\omega \omega_l \\
f_{\lambda,r} \\
f_{\lambda,l} \\
\left(\dot{x}_1 \ddot{y}_1 - \dot{y}_1 \ddot{x}_1\right)/\left(\dot{y}_1^2 + \dot{x}_1^2\right) \\
\left(\dot{x}_2 \ddot{y}_2 - \dot{y}_2 \ddot{x}_2\right)/\left(\dot{y}_2^2 + \dot{x}_2^2\right) \\
\left(\dot{x}_3 \ddot{y}_3 - \dot{y}_3 \ddot{x}_3\right)/\left(\dot{y}_3^2 + \dot{x}_3^2\right) \\
\left(\dot{x}_4 \ddot{y}_4 - \dot{y}_4 \ddot{x}_4\right)/\left(\dot{y}_4^2 + \dot{x}_4^2\right)
\end{bmatrix}
\tag{20}
$$

and the control input matrix $g(x)$ is

$$
g(x) =
\begin{bmatrix}
0 & 0 & 0 & k_\omega & 0 & g_{\lambda,r} & 0 & 0 & 0 & 0 & 0 \\
0 & 0 & 0 & 0 & k_\omega & 0 & g_{\lambda,l} & 0 & 0 & 0 & 0
\end{bmatrix}^T
\tag{21}
$$

In the obtained control-affine approximated model, the unknown parameters c_i, $i = 0, ..., 4$ and d_i, $i = 1, 2, 3$ will be estimated via an EKF.

5. States and Unknown Parameters' Estimation

Directly measuring the unknown parameters c_i, $i = 0, 1, 2, 3, 4$ and d_i, $i = 1, 2, 3$ in the derived model is challenging. Furthermore, these parameters vary with different terrains, such as loamy soils and sandy soils. To tackle these issues, a hybrid EKF is developed to estimate the unknown parameters of the proposed approximated WTIM, such that the propagated state variables can match experimental data.

The state variables and the unknown parameters to be simultaneously estimated are $x_{ext} = \left[\dot{x}_R, \dot{y}_R, \dot{\psi}_R, \omega_r, \omega_l, c_0, c_1, c_2, c_3, c_4, d_1, d_2, d_3\right]^T$. The measurements obtained from an inertial measurement unit (IMU) and quadrature wheel encoders are $y_{out} = \left[\ddot{x}_R, \ddot{y}_R, \dot{\psi}_R, \omega_r, \omega_l\right]^T$. According to Eqs. (13) and (14), the process model and the measurement model can be expressed, respectively, as

$$
f_{ext}(x_{ext}, u, w) =
\begin{bmatrix}
\dot{\psi}_R \dot{y}_R + 2\left[\sum_{i=0}^{k} c_i\left(\lambda_r^k + \lambda_l^k\right)\right]/m \\
\ddot{y}_R \\
\ddot{\psi}_R \\
-k_\omega \omega_r \\
-k_\omega \omega_l \\
0 \\
0 \\
0 \\
0 \\
0 \\
0 \\
0 \\
0
\end{bmatrix}
+
\begin{bmatrix}
w_1 \\
w_2 \\
w_3 \\
w_4 \\
w_5 \\
w_6 \\
w_7 \\
w_8 \\
w_9 \\
w_{10} \\
w_{11} \\
w_{12} \\
w_{13}
\end{bmatrix}
\tag{22}
$$

Fig. 5. DDAGR in front of a strawberry bed in a commercial strawberry orchard.

and

$$
h(x_{ext}, \mathbf{v}) = \begin{bmatrix} \dot{\psi}_R \dot{y}_R + 2 \left[\sum_{i=0}^{k} c_i \left(\lambda_r^k + \lambda_l^k \right) \right] / m \\ -\dot{\psi}_R \dot{x}_R - d_1 \left[k_r \left(\beta_1 + \beta_3 \right) + k_l \left(\beta_2 + \beta_4 \right) \right] / m \\ \dot{\psi}_R \\ \omega_r \\ \omega_l \end{bmatrix} + \begin{bmatrix} \mathrm{v}_1 \\ \mathrm{v}_2 \\ \mathrm{v}_3 \\ \mathrm{v}_4 \\ \mathrm{v}_5 \end{bmatrix}, \tag{23}
$$

where $\mathbf{w} = [\mathrm{w}_i]_{i=1,\dots,13}$ and $\mathbf{v} = [\mathrm{v}_i]_{i=1,\dots,5}$ are assumed to be zero mean white Gaussian noises with covariances of Q and R, respectively. The yaw rate $\dot{\psi}_R$ and the left and right wheel bank angular velocities, ω_r and ω_l, in Eq. (23) can be directly ascertained from the state estimate. The detailed steps in designing the hybrid EKF can be found in ref. [22].

6. Experiment Validation
A scouting experiment is conducted to validate the EKF algorithm in estimating the state variables and the unknown parameters of the approximated, control affine model. Here, the Disease Detection Agricultural Ground Robot (DDAGR), shown in Fig. 5, is used as the robot platform and is commanded to cover three strawberry rows in a commercial farm. Afterwards, the EKF is run off-line using the data acquired in the experiment.

6.1. DDAGR description
The length of DDAGR is 91.7 cm and its width and height are adjustable to fit different strawberry orchards with dimensions ranging between 146.8−196.8 cm and 82.6−107.6 cm, respectively. For locomotion, DDAGR is equipped with two 24-Volt DC wheelchair motors; for navigation, DDAGR is equipped with an array of onboard sensors including an *InvenSense MPU 6050* and two *US Digital E3* optical quadrature encoders. The control system consists of an *Arduino Mega 2560* in conjunction with a *SuperDroid Encoder Buffer* and a *Dimension Engineering Sabertooth 2×60 amp voltage regulator*. The software installed on the *Arduino* can accomplish three tasks: PID regulation of the wheel shaft angular velocity, orientation estimation of the robot, and data acquisition for the control system. The wheel shaft angular velocity control law and the orientation estimation scheme have a 1 kHz update rate, whereas the raw sensor samples are streamed from the data acquisition portion of the software at 125 Hz. An IMU is placed at the robot center of mass and the optical encoders are placed on the rotor shaft of the DC motors. The physical characteristics of DDAGR are listed in Table III.

6.2. Experiment validation
Experiment is conducted in a sandy loam commercial strawberry farm. The strawberry bed size is about 1 m and the spacing between beds is roughly 0.5 m. The scouting path consists of two phases as shown in Fig. 6. Phase 1 is referred to as the over-bed motion. Here, the robot scouts over the bed along the bed centerline with a constant speed. Phase 2 is referred to as the cross-bed motion, which is further separated as three sections. First, a 90° in-site rotation is taken after the robot passes the

Table III. DDAGR physical properties.

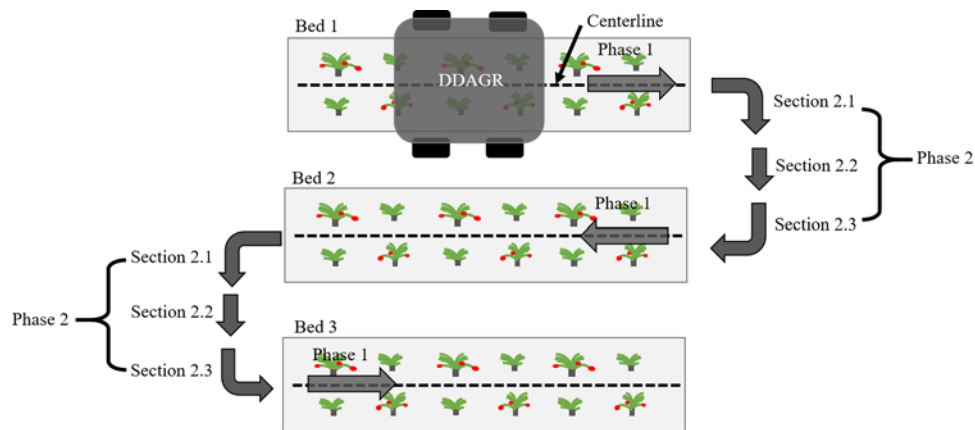| Parameter	Value	Unit	Description
m	185	kg	Robot mass
I_z	100	$kg \cdot m^2$	Moment of inertia about the z-axis
r	28	cm	Wheel radius
W	75	cm	Half of robot width
L	35	cm	Half of robot length

Fig. 6. A scouting path covering three rows in a commercial strawberry farm.

headland of the current row (Phase 2.1). Second, a translation allows DDAGR to move towards the next row (Phase 2.2). Finally, another 90° in-site rotation makes the robot align with the next row (Phase 2.3). A PID controller and a sliding mode controller are applied to the over-bed motion and the cross-bed motion, respectively.[23] The wheel angular velocities are varied at the time instances as listed in Table IV with a time step of $\Delta t = 0.13s$.

The initial error covariance matrix P_0, the process covariance matrix Q, and the measurement covariance matrix R used in the experiment, respectively, are

$$P_0 = diag\{[0.01 \ 0.01 \ 1 \ 0.002 \ 0.002 \ 10 \ 10 \ 10 \ 10 \ 10 \ 10 \ 10 \ 10]\} \qquad (24)$$

$$Q = \begin{cases} diag\{[10 \ 10 \ 600000 \ 100 \ 100 \ 1 \ 1 \ 1 \ 1 \ 1 \ 1 \ 1 \ 1] \times 10^{-5}\}, \ 0\,s \leq t < 118.69\,s \\ diag\{[60000 \ 15000 \ 200000 \ 100 \ 100 \ 1 \ 1 \ 1 \ 1 \ 1 \ 1 \ 1 \ 1] \times 10^{-5}\}, \ 118.69\,s \leq t < 134.16\,s \\ diag\{[40000 \ 10000 \ 10000 \ 10000 \ 10000 \ 1 \ 1 \ 1 \ 1 \ 1 \ 1 \ 1 \ 1] \times 10^{-5}\}, \ 134.16\,s \leq t < 142.35\,s \\ diag\{[40000 \ 40000 \ 250000 \ 10000 \ 10000 \ 1 \ 1 \ 1 \ 1 \ 1 \ 1 \ 1 \ 1] \times 10^{-5}\}, \ 142.35\,s \leq t < 157.3\,s \\ diag\{[40 \ 10 \ 2000 \ 10000 \ 10000 \ 1 \ 1 \ 1 \ 1 \ 1 \ 1 \ 1 \ 1] \times 10^{-5}\}, \ 157.3\,s \leq t < 762.58\,s \\ diag\{[60000 \ 15000 \ 500000 \ 1000 \ 1000 \ 1 \ 1 \ 1 \ 1 \ 1 \ 1 \ 1 \ 1] \times 10^{-5}\}, \ 762.58\,s \leq t < 777.66\,s \\ diag\{[40000 \ 20000 \ 250000 \ 10000 \ 10000 \ 1 \ 1 \ 1 \ 1 \ 1 \ 1 \ 1 \ 1] \times 10^{-5}\}, \ 777.66\,s \leq t < 785.33\,s \\ diag\{[40000 \ 20000 \ 20000 \ 10000 \ 10000 \ 1 \ 1 \ 1 \ 1 \ 1 \ 1 \ 1 \ 1] \times 10^{-5}\}, \ 785.33\,s \leq t < 800.41\,s \\ diag\{[20 \ 1 \ 200 \ 10000 \ 10000 \ 1 \ 1 \ 1 \ 1 \ 1 \ 1 \ 1 \ 1] \times 10^{-5}\}, \ 800.41\,s \leq t < 918.19\,s \end{cases}$$

$$(25)$$

and

$$R = diag\{[0.015 \ 0.1 \ 0.015 \ 10^{-5} \ 10^{-5}]\} \qquad (26)$$

The estimated wheel angular velocities are shown in Fig. 7. It can be seen that the estimated angular velocities track the measurements and match the commands listed in Table IV. Figure 8 shows the measured and estimated longitudinal velocity $\dot{x}_R$, lateral velocity $\dot{y}_R$, and yaw rate $\dot{\psi}_R$. The results indicate that DDAGR starts with an over-bed motion scouting over the first strawberry

Table IV. Wheel bank velocities used in the scouting motion experiment.

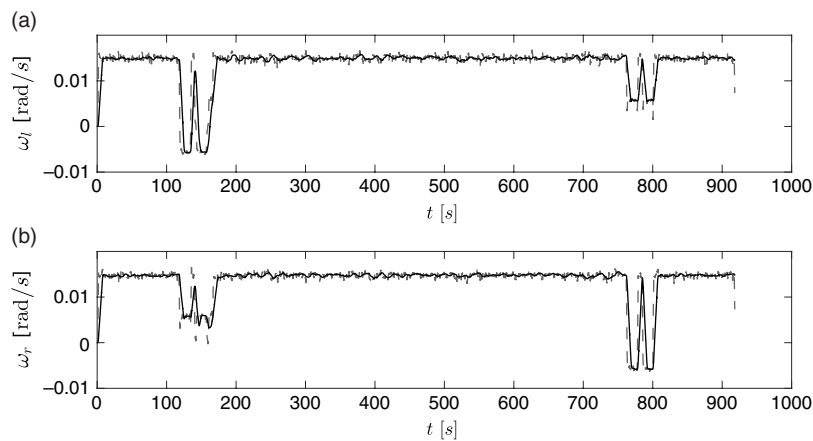| t (s)	ω_r(rad/s)	ω_l(rad/s)
0.00−118.69	0.82	0.82
118.69−134.16	0.32	−0.32
134.16−142.35	0.82	0.82
142.35−157.30	0.32	−0.32
157.30−762.58	0.82	0.82
762.58−777.66	−0.32	0.32
777.66−785.33	0.82	0.82
785.33−800.41	−0.32	0.32
800.41−918.19	0.82	0.82

Fig. 7. Measured and estimated wheel velocities of DDAGR in the scouting motion: (a) left wheel angular velocity and (b) right wheel angular velocity. The dotted and solid lines represent the measurement and estimation, respectively.
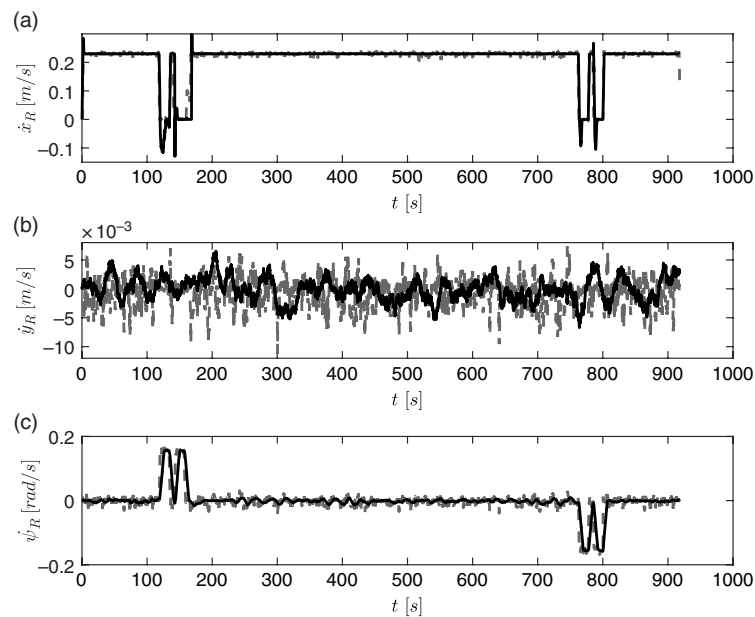

Fig. 8. Measured and estimated velocities of DDAGR in the scouting motion: (a) longitudinal velocity, (b) lateral velocity, and (c) yaw rate, where the dotted and solid lines represent the measurement and estimation, respectively.
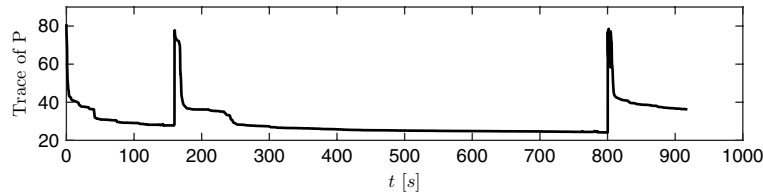
Fig. 9. Trace of the error covariance matrix of DDAGR in the scouting motion.
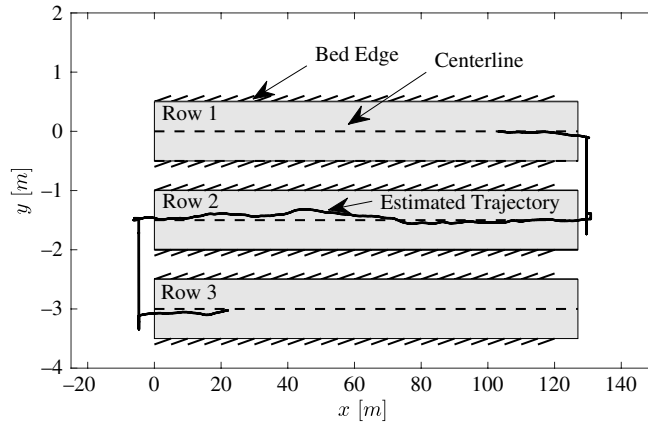

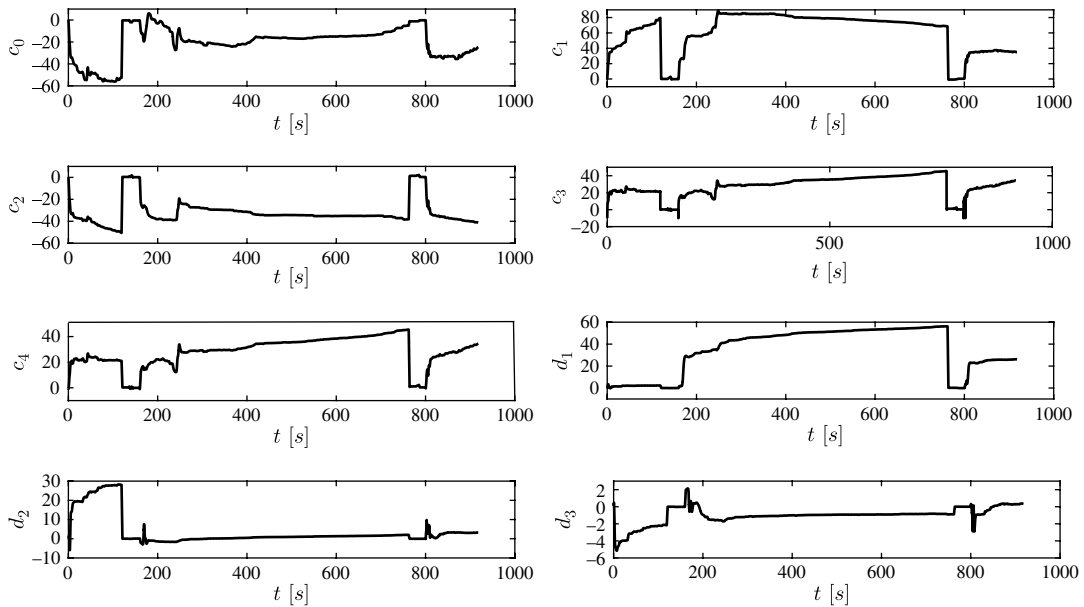Fig. 10. The estimated trajectory of DDAGR in the scouting motion.

Fig. 11. Parameter estimation of DDAGR approximated WTIM in the scouting motion: $\hat{c}_0$, $\hat{c}_1$, $\hat{c}_2$, $\hat{c}_3$, and $\hat{c}_4$ are the parameters in the longitudinal force model, while $\hat{d}_1$, $\hat{d}_2$, and $\hat{d}_3$ are the parameters in the lateral force model.

bed with a longitudinal velocity about 0.23 m/s. At about 120 s, it turns and starts moving towards the second bed. The turning yaw rate is about 0.15 rad/s, and the translation is with a longitudinal velocity around 0.23 m/s. Beginning at 160 s, DDAGR scouts over the second bed with a constant longitudinal velocity of 0.23 m/s. Once it reaches the headland of the second bed at around 790 s, a cross-bed motion with a yaw rate of 0.15 rad/s and a longitudinal velocity of 0.23 m/s allows the robot to move towards the third strawberry bed. From 800 to 920 s, the robot scouts the third strawberry

bed with a longitudinal velocity of 0.23m/s. The trace value of the error covariance matrix is shown in Fig. 9, indicating that the EKF is stable and works properly.

Figure 10 shows the estimated scouting motion trajectory. The estimated trajectory is obtained by integrating the estimated velocities. Referring to Fig. 8, DDAGR moves forward along the centerline of the first bed with a longitudinal velocity of 0.23 m/s. After traveling about 30 m, it reaches the headland of the first bed. The robot moves from the first bed to the second bed between 120 and 160 s, and then starts scouting over the second bed for about 130 m. DDAGR moves towards the third bed from 760 to 800 s, scouts 40 m in the third bed, and then stops.

Figure 11 shows the estimates of unknown parameters of the approximated WTIM $\hat{c}_i$, $i = 0, 1, 2, 3, 4$ and $\hat{d}_i$, $i = 1, 2, 3$. Due to varying terrain and motion conditions, the estimated parameters are stabilized at different values for different sections and phases. However, all these estimated parameters vary within a small range. Therefore, it is not a challenging task to design a proper controller that is robust or adaptive with respect to such parametric uncertainties.

7. Conclusion

In this study, a control affine dynamic model is developed for a ground robot designed to scout throughout commercial strawberry fields. The approximated terramechanic WTIM considers a torus wheel geometry, and a least squares curve fit is applied to obtain a control affine force model. The unknown parameters in the derived model vary depending on terrain conditions, and thus an EKF is designed to estimate those parameters, such that the propagated state variables via the approximated model can match experiment data. A scouting motion experiment covering three rows of strawberry beds in a commercial farm validated the proposed approximated WTIM and the EKF-based parameter estimation method.

Acknowledgments

References

1. L. Ewing, "Strong growth predicted for ground robots designed for agriculture," In: *Mission Critical: Agriculture 2014 by Association for Unmanned Vehicle Systems*, vol. 4, issue no. 2 (2014) pp. 13–15.
2. F. Dong, W. Heinemann and R. Kasper, "Development of a row guidance system for an autonomous robot for white asparagus harvesting," *Comput. Electron. Agric.* **79**(2), 216–225 (2011).
3. J. P. Fentanes, I. Gould, T. Duckett, S. Pearson and G. Cielniak, "3D soil compaction mapping through kriging-based exploration with a mobile robot," *arXiv preprint* arXiv:1803.08069 (2018).
4. S. Hayashi, K. Shigematsu, S. Yamamoto, K. Kobayashi, Y. Kohno, J. Kamata and M. Kurita, "Evaluation of a strawberry-harvesting robot in a field test," *Biosyst. Eng.* **105**(2), 160–171 (2010).
5. K. V. Asefpour and J. Massah, "Design, development and performance evaluation of a robot to early detection of nitrogen deficiency in greenhouse cucumber (Cucumis sativus) with machine vision," *Int. J. Agric.: Res. Rev.* **2**(4), 448–454 (2012).
6. S. Sankaran, A. Mishra, R. Ehsani and C. Davis, "A review of advanced techniques for detecting plant diseases," *Comput. Electron. Agric.* **72**(1), 1–13 (2010).
7. G. Campion, G. Bastin and B. D'Andréa-Novel, "Structural properties and classification of kinematic and dynamic models of wheeled mobile robots," *IEEE Trans. Robot. Autom.* **12**(1), 47–62 (1996).
8. C. Ton, Z. Kan and S. S. Mehta, "Obstacle avoidance control of a human-in-the-loop mobile robot system using harmonic potential fields," *Robotica* **36**(4), 463–483 (2018).
9. L. Caracciolo, A. D. Luca and S. Iannitti, "Trajectory tracking control of a four-wheel differentially driven mobile robot," In: *Proceedings of IEEE International Conference on Robotics and Automation* (1999) pp. 2632–2638.
10. J. Yi, H. Wang, J. Zhang, D. Song, S. Jayasuriya and J. Liu, "Kinematic modeling and analysis of skid-steered mobile robots with applications to low-cost inertial-measurement-unit-based motion estimation," *IEEE Trans. Robot.* **25**(5), 1087–1097 (2009).
11. F. Wu, Z. Guan and A. Whidden, "Strawberry industry overview and outlook," Unpublished manuscript, Gulf Coast Research and Education Center, University of Florida, Gainesville, Florida. Retrieved from http://www.fred.ifas.ufl.edu/pdf/webinar/Strawberry.pdf (2012).
12. M. G. Bekker, *Theory of Land Locomotion* (University of Michigan Press, 1956).
13. J. Y. Wong, *Theory of Ground Vehicles* (John Wiley & Sons, Hoboken, New Jersey, 2001).
14. Z. Jia, W. Smith and H. Peng, "Terramechanics-based wheel–terrain interaction model and its applications to off-road wheeled mobile robots," *Robotica* **30**(3), 491–503 (2011).

15. G. Ishigami, A. Miwa, K. Nagatani and K. Yoshida, "Terramechanics-based model for steering maneuver of planetary exploration rovers on loose soil," *J. Field Robot.* **24**(3), 233–250 (2007).
16. A. Gray, E. Abbena and S. Salamon, *Modern Differential Geometry of Curves and Surfaces with Mathematica*, 3rd edn. (CRC press, 2006).
17. J. Y. Wong and A. R. Reece, "Prediction of rigid wheel performance based on the analysis of soil-wheel stresses part I. performance of driven rigid wheel," *J. Terramech.* **4**(1), 81–88 (1967).
18. T. H. Tran, N. M. Kwok, S. Scheding and Q. P. Ha, "Dynamic modeling of wheel-terrain interaction of a UGV," In: *Proceedings of the 3rd IEEE International Conference on Automation Science and Engineering* (2007) pp. 369–374.
19. C. C. Ward and K. Iagnemma, "A dynamic-model-based wheel slip detector for mobile robots on outdoor terrain," *IEEE Trans. Robot.* **24**(4), 821–831 (2008).
20. O. Onafeko and A. R. Reece, "Soil stresses and deformations beneath rigid wheels," *J. Terramech.* **4**(1), 59–80 (1967).
21. J. Yi, D. Song, J. Zhang and Z. Goodwin, "Adaptive trajectory tracking control of skid-steered mobile robots," In: *Proceedings of IEEE International Conference on Robotics and Automation* (2007) pp. 2605–2610.
22. D. Simon, *Optimal State Estimation: Kalman, H Infinity, and Nonlinear Approaches* (John Wiley & Sons, Inc., Hoboken, New Jersey, 2006).
23. D. Freese and Y. Xu, "Nonlinear robust path control for a field robot scouting in strawberry orchards," In: *Proceedings of the ASME Dynamic Systems and Controls Conference* (2017) pp. V002T21A006.
24. C. J. Willmott and K. Matsuura, "Advantages of the mean absolute error (MAE) over the root mean square error (RMSE) in assessing average model performance," *Climate Research* **30**(1), 79–82 (2005).
25. D. N. Gujarati and D. C. Porter, *Basic Econometrics*, 5th edn. (The McGraw–Hill, New York, United States, 2008) pp. 73–78.

Appendix A. Terramechanics

A.1. Integral bounds

For clarity and completeness of the study, a brief derivation of terramechanic pressure equations adopted from refs. [13] and [14] are listed here.

The first relationships between the entry and exit angles, θ_f and θ_r, to the entry depth h_f are established for a wheel rolling horizontally on a plane. The entry angle θ_f can be computed using

$$\theta_f = \cos^{-1}\left(1 - \left[h_f / (c + a)\right]\right) \tag{A1}$$

and the exit angle θ_r is

$$\theta_r = \theta_f \lambda_\theta, \tag{A2}$$

in which λ_θ is the terrain compressibility ratio. The right and left bound angle ψ_r and ψ_l are computing using

$$\psi_l = \cos^{-1}\left(1 - h_f / a\right) \tag{A3}$$

and

$$\psi_r = -\psi_l \tag{A4}$$

The sinkage depth h_f in the above equations is solved for using the search algorithm shown in ref. [22].

A.2. Normal stress

The normal stress equation used in the model is

$$\sigma_n(\theta, \psi) = \left(k_c / b_\psi + k_\phi\right) r_\psi^n \bar{\theta}^n, \tag{A5}$$

in which n is the exponential coefficient, k_c is the cohesion factor, and k_ϕ is the angle of cohesion factor. The term $r_\psi \bar{\theta}$ represents the effective location along the wheel. The radius of a vertical wheel slice r_ψ can be found using

$$r_\psi = c + a \cos\psi \tag{A6}$$

The modified angle $\bar{\theta}$ is defined as

$$\bar{\theta} = \begin{cases} \cos\theta - \cos\theta_f, & \theta_m \leq \theta < \theta_f \\ \cos\left\{\theta_f - \left[(\theta - \theta_r/\theta_m - \theta_r)\right](\theta_f - \theta_m)\right\} - \cos\theta_f, & \theta_r < \theta \leq \theta_m \end{cases}, \tag{A7}$$

in which θ_m is the point with the maximum normal stress, specified by the terrain properties a_0 and a_1 in the equation of

$$\theta_m = (a_0 + a_1\lambda)\,\theta_f, \tag{A8}$$

where λ is the wheel slip ratio. In Eq. (A5), b_ψ is the effective width of the tire at point on the surface which can be found using

$$b_\psi = 2b\sin\psi \tag{A9}$$

A.3. Shear stress

The shear stress along the contact patch is a function of the shear deformation j that the wheel has done on the terrain and the normal stress σ that the wheel imparts on the terrain.

$$\tau\,(\sigma,\,j) = \tau_m\left(1 - e^{-j/K}\right), \tag{A10}$$

where j is the magnitude of the shear deformation of the terrain along the contact patch, namely $j = |\boldsymbol{j}| = \sqrt{j_l^2 + j_t^2}$. Note that j_t is the tangential deformation, j_l is the lateral deformation, and the normal deformation j_n is assumed to be zero. The lateral and shear deformations will be derived later in this appendix. K is the shear modulus, a constant terrain property parameter, and τ_m is the maximum shear stress which is a function of the normal stress and can be computed by

$$\tau_m = c_m + \sigma\tan\phi, \tag{A11}$$

which is dictated by the terrain cohesion property c_m and the terrain angle cohesion property ϕ.

The shear stress in Eq. (A10) is broken into the lateral and tangential components using the approach in ref. [14], where the shear velocity vector, $\left[v_{jt}\ v_{jl}\ v_{jn}\right]^T$, is utilized to separate the tangential and lateral components as

$$\tau_t(\sigma,\,j) = \tau_t\,(\sigma,\,j)\left(v_{jt}/\sqrt{v_{jt}^2 + v_{jl}^2}\right) \tag{A12}$$

and

$$\tau_t(\sigma,\,j) = \tau_t\,(\sigma,\,j)\left(v_{jl}/\sqrt{v_{jt}^2 + v_{jl}^2}\right) \tag{A13}$$

The shear velocities of the wheel surface $\left[v_{jt}\ v_{jl}\ v_{jn}\right]^T$ are the lateral and tangential components of the absolute wheel velocity at any point along the wheel surface. Suppose the velocity of wheel hub center is $\left[v_x, v_y, v_z\right]^T$ and its angular velocity is $\left[\omega_x, \omega_y, \omega_z\right]^T$, then the absolute velocity of an arbitrary point $\left[x, y, z\right]^T$ on the wheel surface is

$$\boldsymbol{v}(\psi, \theta) = \begin{bmatrix} \tilde{v}_x \\ \tilde{v}_y \\ \tilde{v}_z \end{bmatrix} = \begin{bmatrix} v_x + \omega_y z - \omega_z y \\ v_y - \omega_x z + \omega_z x \\ v_z + \omega_x y - \omega_y x \end{bmatrix} \tag{A14}$$

The lateral and tangential components of the absolute wheel velocity can be expressed as

$$v_{jt} = \tilde{v}_x\cos\theta - \tilde{v}_z\sin\theta \tag{A15}$$

$$v_{jl} = \tilde{v}_x\sin\psi\sin\theta + \tilde{v}_y\cos\psi + \tilde{v}_z\sin\psi\cos\theta, \tag{A16}$$

and

$$v_{jn} = \tilde{v}_x\cos\psi\sin\theta - \tilde{v}_y\sin\psi + \tilde{v}_z\cos\psi\cos\theta \tag{A17}$$

Table A1. Terramechanic WTIM parameter description and values for DDAGR.

Parameter	Value	Unit	Description
a	5.0	cm	Minor radius
a_0	0.5	–	Coefficient for θ_m
a_1	0.5	–	Coefficient for θ_m
b	10.16	cm	Half of the wheel width
c	22.94	cm	Major radius
c_m	4140	Pa	Cohesion coefficient
K	0.006	m	Shear modulus
k_c	13,190	N/m^{n+1}	Cohesive modulus
k_ϕ	692,000	N/m^{n+1}	Friction modulus
n	0.5	–	Exponential coefficient
λ_θ	0.9	–	Coefficient for θ_r
ϕ	13	deg	Internal friction angle

The shear deformation of terrain j that has occurred at a point along the wheel–terrain contact patch can be calculated by integrating the shear rate over time. In the terramechanic WTI models, if we assume that the states rolling on horizontal ground are quasi-steady, the velocity v and the angular rate ω at the wheel hub can be treated as constants during a brief time interval of the integration. The shear deformation of the terrain j in the lateral and tangential directions can be calculated by using

$$j_t\,(\psi,\theta) = \left[\tilde{v}_x\,(\sin\theta_f - \sin\theta) + \tilde{v}_z\,(\cos\theta_f - \cos\theta)\right]/\omega_y \tag{A18}$$

and

$$j_l\,(\psi,\theta) = \left[k_1\tilde{v}_x\sin\psi + \tilde{v}_y\,(\theta_f - \theta)\cos\psi + k_2\tilde{v}_z\sin\psi\right]/\omega_y, \tag{A19}$$

where $k_1 \triangleq \cos\theta - \cos\theta_f$ and $k_2 \triangleq \sin\theta_f - \sin\theta$.

The soil parameters used to simulate the off-road environments are listed in Table A1.

Appendix B. Nomenclatures

a	minor radius of the wheel
a_i	coefficients for the angle of the point with the maximum normal stress, $i = 0, 1$
b	half of the wheel width
b_ψ	effective width of the wheel
c	major radius of the wheel
c_i	coefficients of the approximated longitudinal force, $i = 0, 1, 2, 3, 4$
c_m	coefficient of the terrain cohesion
d_i	coefficients of the approximated lateral force, $i = 1, 2, 3$
$F_{w,i}$	wheel–terrain interaction forces, $i = x, y$
$\boldsymbol{f}$	state function in the control affine model
$\boldsymbol{f_{ext}}$	state function in the process model
$\boldsymbol{g}$	control input matrix in the control affine model
h_f	entry sinkage depth
h_r	exit sinkage depth
$\boldsymbol{h}$	measurement model
I_z	moment of inertia about the z-axis
$\boldsymbol{j}$	shear deformation vector, $\boldsymbol{j} = \left[j_t,\,j_l,\,j_n\right]^T$
K	shear modulus of the soil
k_c	cohesive modulus of the soil
k_ω	motor time constant of the PID controller
k_ϕ	friction modulus of the soil
L	half of the robot length
$\boldsymbol{M_{ext}}$	moment about the z-axis of the robot
m	mass of the robot

P_0	initial error covariance matrix
Q	covariance matrix of the noise in the process model
R	covariance matrix of the noise in the measurement model
r	wheel radius
$\boldsymbol{r_p}$	position vector of an arbitrary point on the wheel surface
r_ψ	radius of a vertical wheel slice
t	time
$\boldsymbol{u}$	control variable
$\boldsymbol{v}$	absolute velocity of an arbitrary point on the wheel surface
$\mathbf{v}$	zero mean white Gaussian noise associated with the measurement model
W	half of the robot width
$\mathbf{w}$	zero mean white Gaussian noise associated with the process model
x_R	longitudinal position in the body fixed frame
$\dot{x}_R$	longitudinal velocity in the body fixed frame
$\ddot{x}_R$	longitudinal acceleration in the body fixed frame
$\boldsymbol{x}$	state vector in the control affine model
$\dot{x}_i$	longitudinal velocity of the ith wheel in the wheel frame, $i = 1, 2, 3, 4$
$\ddot{x}_i$	longitudinal acceleration of the ith wheel in the wheel frame, $i = 1, 2, 3, 4$
$\boldsymbol{x_{ext}}$	state vector to be estimated
y_R	longitudinal position in the body fixed frame
$\boldsymbol{y_{out}}$	measurement vector
$\dot{y}_R$	longitudinal velocity in the body fixed frame
$\ddot{y}_R$	longitudinal acceleration in the body fixed frame
$\dot{y}_i$	longitudinal velocity of the ith wheel in the wheel frame, $i = 1, 2, 3, 4$
$\ddot{y}_i$	longitudinal acceleration of the ith wheel in wheel fixed frame, $i = 1, 2, 3, 4$
β_i	slip angle of the ith wheel, $i = 1, 2, 3, 4$
θ	rotation angle of the wheel
θ_f	entry angle
θ_r	exit angle
θ_m	angle of the point with the maximum normal stress
λ_i	the ith wheel slip ratio, $i = r, l, 1, 2, 3, 4$
$\dot{\lambda}_i$	rate of change of the ith wheel slip ratio, $i = r, l$
λ_θ	coefficient for θ_r
$\boldsymbol{\rho_i}$	position vector from the center of mass of the robot to the origin of the wheel local reference frame
σ_n	normal stress along the wheel–terrain contact surface
τ_i	shear stresses along the wheel–terrain contact surface, $i = t, l$
τ_m	maximum shear stress of the wheel
ϕ	internal friction angle of the soil
ψ_i	bound angles of the wheel with respect to the soil, $i = r, l$
ψ_R	heading angle of the robot
$\dot{\psi}_R$	yaw rate of the robot
$\ddot{\psi}_R$	yaw acceleration of the robot
Ω_I	inertial reference frame
Ω_B	body fixed reference frame
Ω_i	wheel local reference frame
Ω_H	wheel hub reference frame
Ω_S	wheel surface reference frame
ω_i	the ith wheel angular velocity, $i = r, l, 1, 2, 3, 4$
$\omega_{c,i}$	commanded angular velocities of the wheel banks, $i = r, l$
$\dot{\omega}_i$	angular acceleration of the wheel banks, $i = r, l$